Design of Parallel Transmission Radiofrequency Pulses Robust Against Respiration in Cardiac MRI at 7 Tesla

Sebastian Schmitter,* Xiaoping Wu, Kâmil Uğurbil, and Pierre-François Van de Moortele

Purpose: Two-spoke parallel transmission (pTX) radiofrequency (RF) pulses have been demonstrated in cardiac MRI at 7T. However, current pulse designs rely on a single set of B_1^+/B_0 maps that may not be valid for subsequent scans acquired at another phase of the respiration cycle because of organ displacement. Such mismatches may yield severe excitation profile degradation.

Methods: B_1^+/B_0 maps were obtained, using 16 transmit channels at 7T, at three breath-hold positions: exhale, half-inhale, and inhale. Standard and robust RF pulses were designed using maps obtained at exhale only, and at multiple respiratory positions, respectively. Excitation patterns were analyzed for all positions using Bloch simulations. Flip-angle homogeneity was compared in vivo in cardiac CINE acquisitions.

Results: Standard one- and two-spoke pTX RF pulses are sensitive to breath-hold position, primarily due to B_1^+ alterations, with high dependency on excitation trajectory for two spokes. In vivo excitation inhomogeneity varied from nRMSE = 8.2% (exhale) up to 32.5% (inhale) with the standard design; much more stable results were obtained with the robust design with nRMSE = 9.1% (exhale) and 10.6% (inhale).

Conclusion: A new pTX RF pulse design robust against respiration induced variations of B_1^+/B_0 maps is demonstrated and is expected to have a positive impact on cardiac MRI in breath-hold, free-breathing, and real-time acquisitions. **Magn Reson Med 74:1291–1305, 2015. © 2014 Wiley Periodicals, Inc.**

Key words: 7 Tesla; cardiac MRI; respiration; breath-hold; pTX; spoke pulses; RF pulse design

INTRODUCTION

MRI of the heart is a challenging task, primarily due to cardiac and respiratory motion. However, significant advances in the fast-growing field of cardiovascular magnetic resonance (CMR) have facilitated overcoming many of these problems. Cardiac motion is typically addressed by synchronizing MR data acquisition with the cardiac cycle using a physiological triggering device. Respiratory motion can be addressed in different ways. A common approach consists of acquiring cardiac images during breath-holds (1). Alternatively, cardiac images can be obtained during free-breathing using, in most cases, navigator scans to monitor the respiration cycle (2). Recent efforts have been made to increase the time efficiency of free-breathing acquisitions (3), and even faster acquisition schemes open the door to real-time cardiac imaging (4,5).

In parallel to these efforts toward faster acquisition, there is an increasing interest in using a higher magnetic field strength (3T) for CMR (6), despite well-known challenges such as banding artifacts, higher specific absorption rate (SAR), and flip angle nonuniformity (7,8). Furthermore, several groups are investigating the use of ultrahigh field scanners (7T and higher) for CMR (9–13) to take advantage of higher signal-to-noise ratio (14), increased parallel imaging performance (15), and longer T_1 relaxation constants (10,16), with the perspective of increasing spatial and temporal resolution, shortening acquisition time, or obtaining better contrast. However, one of the major challenges, particularly when imaging the human torso, consists of spatial inhomogeneity of radiofrequency (RF) excitation profiles due to shorter RF wavelength, which results in undesirable spatial variations of tissue contrast (14,17). A promising technique to address this issue relies on parallel transmission (pTX) methods using multiple transmit RF channels (18,19).

We have previously demonstrated B_1^+ shimming (13) as well as two-spoke pTX RF pulse design in the heart at 7T, with improved excitation homogeneity obtained with the two-spoke design compared with the one-spoke design with the same RF energy (20). As discussed in the latter reference, a reduction in signal amplitude was observed in two subjects in the left ventricle in four-chamber view with two-spoke RF pulses, and it was hypothesized that blood flow was a likely cause of this effect. Because this study was then expanded to a larger population, similar deviations between predicted and measured excitation profiles occurred again in some subjects and, in the case of two-spoke pulses, these deviations clearly depended on the particular k-space trajectory that was used. Further investigation revealed that these subjects did not succeed in holding their breath at the same position of the respiration cycle between different breath-hold scans acquired during a same session. Hence, the B_1/B_0 calibration scans may have been obtained at a different respiratory position than subsequent cardiac scans for which pTX RF pulses were designed. However, changes in the respiration

University of Minnesota, Center for Magnetic Resonance Research, Minneapolis, Minnesota, USA.

Grant sponsor: National Institutes of Health; Grant numbers: S10 RR26783; P41 EB015894; R21 EB009138; R01-EB006835; R01-EB007327; Grant sponsor: The W. M. Keck Foundation.

*Correspondence to: Sebastian Schmitter, Ph.D., Center for Magnetic Resonance Research, University of Minnesota Medical School, 2021 6th Street SE, Minneapolis, MN 55455. E-mail: sschmitt@umn.edu

Received 12 June 2014; revised 15 September 2014; accepted 13 October 2014

DOI 10.1002/mrm.25512

Published online 19 November 2014 in Wiley Online Library (wileyonlinelibrary.com).

© 2014 Wiley Periodicals, Inc.

position alter the transmit B_1 (B_1^+) distribution, as has been demonstrated at 3T in the liver (21,22), which may impact the pTX RF excitation fidelity.

In the current study, we explored the impact of respiration on one- and two-spoke pTX RF pulse design for CINE cardiac imaging at 7T. We present modified calibration sequences that acquire B_1^+ (or B_0) calibration data and diaphragm images in an interleaved fashion to identify the respiratory position during the calibration scan. Finally, we propose a new pTX RF pulse design, which allows calculating pTX RF pulses robust against respiration. The general framework introduced in this study can also be applied to free-breathing and real-time acquisitions.

THEORY

Conventional Spoke Pulse Design and Respiratory Positions

Two-spoke pTX RF pulses for cardiac CINE imaging were designed by solving a minimization problem in the small tip angle regime similar to (20), based on the spatial domain method (23), using a magnitude least squares optimization (24):

$$\hat{\mathbf{b}} = \text{argmin}\left(|||\mathbf{Ab}| - |\mathbf{m}|||_w^2 + R(\mathbf{b}) \right) \quad [1]$$

The fidelity term $|||\mathbf{Ab}| - |\mathbf{m}|||_w^2$ denotes the quadratic deviation between the magnitude of the actual excitation pattern $\mathbf{Ab}$ and the target excitation pattern $\mathbf{m}$ (here $\mathbf{m}$ is constant throughout the region of interest). $\mathbf{A}$ is the concatenated system matrix including $n = 1 \ldots N$ spatial points, $k = 1 \ldots K$ transmit channels, and $s = 1 \ldots S$ spokes. Each element of the $N \times (K \times S)$ matrix $\mathbf{A}$ can be expressed as:

$$a_{n,k+(s\text{-}1)\cdot K} = i\gamma m_0 \Delta T \cdot B_{1,k}^+(\mathbf{r_n}) \cdot e^{i\gamma \Delta B_0(\mathbf{r_n})[t_s\text{-}T]} e^{2\pi i \cdot \mathbf{r_n} \cdot \mathbf{k}(t_s)}, \quad [2]$$

where $\mathbf{r_n}$ represents the spatial coordinates, $B_{1,k}^+(\mathbf{r_n})$ represents the spatial transmit B_1 sensitivity profiles, $\mathbf{k}(t_s)$ represents the spokes' k-space positions, t_s is the time at the center of each spoke RF pulse, T is the total pulse duration, ΔT is the duration between two subpulses, ΔB_0 ($\mathbf{r_n}$) represents the deviations of the magnetic field B_0, γ is the proton gyromagnetic ratio, and m_0 is the equilibrium magnetization. Accordingly, the vector $\mathbf{b}$ denotes the $S \times K$ complex weights for S spokes and K transmit elements (here $S = 2$ and $K = 16$). In this study, the regularization term $R(\mathbf{b})$ in Equation [1] is defined as $R(\mathbf{b}) = \lambda^2 ||\mathbf{b}||^2$, which includes the total RF energy represented by $||\mathbf{b}||^2$ weighted by a squared regularization parameter λ.

After RF pulse calculation, the flip angle (FA) map $\alpha(\mathbf{r})$, corresponding to the optimized result $\hat{\mathbf{b}}$, is calculated using a Bloch simulation denoted by f_{Bloch}:

$$\alpha(\mathbf{r}) = f_{Bloch}(\hat{\mathbf{b}}, B_{1,k}^+, \Delta B_0) \quad [3]$$

Consistency between Bloch simulation (based on ΔB_0 and B_1^+ calibration maps) and experimental results is routinely used as an internal validation. However, alteration of B_1^+ and/or ΔB_0 occurring between the reference calibration scan and the actual imaging scan with optimized pTX RF pulses can result in excitation pattern deviations (21). Therefore, deviations of the pTX excitation pattern may occur when subsequent scans are not acquired at the same position of the respiratory cycle compared with the calibration maps used as reference.

In this study, we considered three different respiratory positions: end-exhalation (exhale), full inhalation (inhale), and half-inhale, with ΔB_0 and B_1^+ calibration maps being experimentally measured in each position. In the following, we consider the situation where an RF pulse, designed based on calibration maps acquired at position $p_{\text{reference}}$, is actually applied during a scan at p_{actual}. The resulting excitation pattern becomes:

$$a(\mathbf{r})|_{p_{\text{actual}}}^{p_{\text{reference}}} = f_{Bloch}(\hat{\mathbf{b}}|_{p_{\text{reference}}}, B_{1,k}^+|_{p_{\text{actual}}}, \Delta B_0|_{p_{\text{actual}}}) \quad [4]$$

Throughout the study, only the reference calibration maps obtained at exhale were used for the "conventional" RF pulse design.

Robust RF Pulse Design

Ideally, an optimized RF pulse should preserve satisfactory excitation homogeneity even if applied at another point of the respiratory cycle than the reference calibration. A possible formulation to achieve this goal is to design an RF pulse that is simultaneously satisfactory on $\tilde{P}$ different respiratory positions. Hence, we propose when solving Equation [1] to define the excitation target as the union of the regions of interest (ROIs) over the heart at those $\tilde{P}$ different respiratory positions. In this study, we consider $\tilde{P} = 2$ positions: exhale and inhale. To further determine whether using only two calibration positions to design more robust RF pulses provides satisfactory results at other respiratory positions, we also collected ΔB_0 and B_1^+ maps at half-inhale to perform Bloch simulations at $P = 3$ different positions. In practice, designing robust RF pulses for single-slice excitation over $\tilde{P}$ positions is realized in analogy to (25), where RF pulses for a slab selective excitation were optimized simultaneously based on multiple calibration slices. For the robust design, matrix $\mathbf{A}$ is expanded along the spatial dimension as if $\tilde{P}$ virtual slices (i.e. for $\tilde{P}$ different respiratory positions) were considered in lieu of a single slice position, with ROI w_i and magnetization m_i specific to each corresponding ROI, with $i = 1, \ldots, \tilde{P}$:

$$\mathbf{A}_{\text{virtual}} = \begin{bmatrix} \mathbf{A}_1 \\ \mathbf{A}_2 \\ \vdots \\ \mathbf{A}_{\tilde{P}} \end{bmatrix}, \; \mathbf{m}_{\text{virtual}} = \begin{bmatrix} \mathbf{m}_1 \\ \mathbf{m}_2 \\ \vdots \\ \mathbf{m}_{\tilde{P}} \end{bmatrix}, \; w_{\text{virtual}} = w_1 \cup w_2 \ldots \cup w_{\tilde{P}} \quad [5]$$

with:

$$\hat{\mathbf{b}}_{\text{virtual}} = \text{argmin}\left(|||\mathbf{A}_{\text{virtual}}\mathbf{b}| - |\mathbf{m}_{\text{virtual}}|||_{w_{\text{virtual}}}^2 + R(\mathbf{b}) \right). \quad [6]$$

The FA map expected at a respiration position p_{actual} is given by $a(\mathbf{r})|_{p_{\text{actual}}}^{p_{\text{reference}}}$ with $p_{\text{reference}}$ representing the

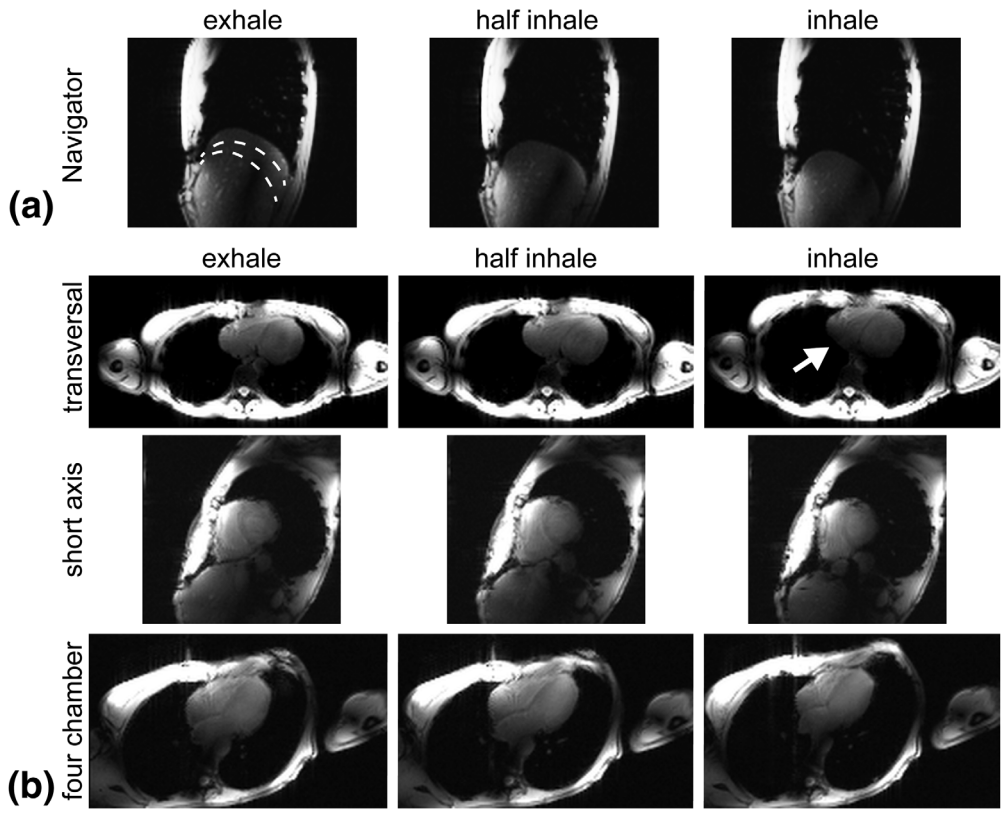

FIG. 1. **a:** Navigator images acquired for three different respiratory positions. The dashed lines in the leftmost image indicate the respective diaphragm position in the two other respiratory states. **b:** Magnitude images obtained from B_0 acquisitions in the same respiratory positions corresponding to panel a for transverse, short axis, and four-chamber view. All images were acquired using a static B1+ phase shim, which minimized B1+ heterogeneity for the exhale position in transverse view. The heterogeneity obtained by this shim setting is not maintained for the inhale position, as indicated by the white arrow.

combined $\tilde{P}$ virtual slice positions. In this study, we demonstrate the robust RF pulse design by performing a simultaneous optimization on $\tilde{P} = 2$ positions (exhale and inhale) while resulting FA maps are simulated with Bloch simulations for $P = 3$ positions: $a(\mathbf{r})|_{exhale}^{(exhale,inhale)}$, $a(\mathbf{r})|_{half\text{-}inhale}^{(exhale,inhale)}$ and $a(\mathbf{r})|_{inhale}^{(exhale,inhale)}$.

METHODS

System and Setup

All experiments were performed on a whole body 7T magnet equipped with a prototype 16-channel pTX system (Siemens AG, Erlangen, Germany). A 16-channel transmit/receive body coil (26) was used, consisting of one posterior and one anterior eight-element arrays. Five subjects who signed a consent form approved by the local Institutional Review Board were scanned. The cardiac cycle was recorded using an electrocardiogram (ECG) with three electrodes attached to the subject's chest. The average heart rates for subjects 1–4 were 53, 64, 65, and 60 beats per minute, whereas subject 5 had a significantly higher heart rate of 96 beats per minute. Using an ECG at 7T is challenging due to the magnetohydrodynamic effect (12); therefore, the electrodes were repositioned whenever cardiac triggering was not satisfactory. Scans were acquired in three orientations: transversal, short axis and pseudo four-chamber view. All computations were performed using MATLAB (MathWorks, Natick, Massachusetts, USA).

Respiratory Controlled Calibration Scans

Throughout this study, we considered the aforementioned three respiratory positions, except in one subject for whom a fourth position between inhale and exhale was used. For each position, calibration datasets including B_1^+ sensitivity profiles of the $K = 16$ TX channels and spatial maps of ΔB_0 were acquired. For each slice orientation, these cardiac-gated calibration scans were performed during one breath-hold in a single slice.

B_1^+ maps were obtained using a modified fast B_1^+ estimation technique as described by Van de Moortele and Ugurbil (27). It sequentially acquires 16 cardiac-gated small flip angle gradient echo (GRE) images during a single breath-hold with only one TX channel activated per image and all channels enabled for reception. The following parameters were used in subjects 1–4: echo time (TE)/pulse repetition time (TR) = 2.6/4.7 ms; bandwidth = 801 Hz/pixel; matrix = 160 × 104; resolution = 2.8 × 2.8 × 5 mm^3. Each one of the 16 GRE images lasted for 436 ms and was acquired during the diastole of a single heartbeat. This short acquisition duration allowed for acquiring a second single-slice image during systole within the same heartbeat, in a sagittal view crossing the diaphragm dome (see Fig. 1a). Thus, the diaphragm position was recorded

16 times, allowing for accurate retrospective verification of respiratory position during B_1^+ calibration. The same acquisition was performed in subject 5, but due to the higher heart rate the bandwidth was increased to 1420 Hz/Px, resulting in an acquisition time per image of 270 ms.

B_0 mapping was performed in a similar way for each respiratory position and each orientation using a cardiac-gated dual-TE GRE acquisition performed under breath-hold. Either of the two phase images was acquired during a single cardiac cycle interleaved by one cardiac cycle used for collecting a sagittal navigator image. ΔB_0 maps were averaged over three acquisitions using the following parameters: TE1/TE2/TR = 3.1/4.1/4.7 ms; bandwidth = 919 Hz/pixel; matrix = 160 × 104; resolution = 2.8 × 2.8 × 5 mm^3.

A third calibration scan was performed targeting only the diaphragm. During this nontriggered acquisition, the subject was asked to slowly but deeply breathe in and out for several breathing cycles. The following parameters were used: TE/TR = 2.3 ms/4.1s; bandwidth = 1488 Hz/pixel; matrix = 160 × 160; resolution = 2.8 × 2.8 × 5 mm^3. This series of images, covering the entire spectrum from end-exhalation to end-inspiration, was used as a reference to determine a posteriori the respiratory position of other scans.

Conventional and Robust RF Pulse Design

For each orientation, three ROIs covering the heart, denoted by w_{exhale}, $w_{\text{half-inhale}}$, and w_{inhale}, were manually drawn based on B_1^+ calibration data obtained at the corresponding respiratory position. Conventional one-spoke and two-spoke RF pulses were designed based on Equation [1] using calibration maps obtained at p_{exhale}. The two spokes were placed symmetrically with respect to $k_x = k_y = 0$ and played out along the k_z axis. The "spokes axis," which is defined by the connecting line from spoke 1 to spoke 2 (compare dashed line in Fig. 5b), was rotated by an angle φ varying from 0° to 360° in 10° steps, whereas the spoke radius $k_r = |\frac{\gamma}{2\pi}\int \mathbf{G}\,dt|$ varied from 0 to 10 m^{-1} in 1 m^{-1} steps. RF pulses were designed for each of the resulting 361 two-spoke trajectories, using two 800-μs long, SINC-shaped RF subpulses with a bandwidth time product (BWTP) of 4 in combination with a slice selection gradient achieving 5-mm slice thickness. The one-spoke RF pulses were played out along k_z at $k_x = k_y = 0$ and the optimization was performed using 361 different starting phase patterns (25) for the target vector $\mathbf{m}$ (yielding same number of solutions as for two spokes). The same SINC-shaped RF pulse with BWTP = 4 was used as the two-spoke subpulse, but the duration was stretched to 1600 μs to maintain the same total duration.

Robust RF pulses were designed based on Equation [6], using calibration data derived from both exhale and inhale position (see the Theory section), whereas RF pulse duration, shape, and BWTP were kept unchanged.

For each solution, the normalized energy E_n (20,25) was calculated by normalizing the total pulse energy $||\mathbf{b}||^2$ by the square of the average value of the FA over the ROI of the reference calibration, denoted by $\text{mean}|\mathbf{Ab}|_{w_{\text{reference}}}$. The maximum energy per channel $E_{\max} = \max(E_k)$, was calculated for each solution. FA maps $a(\mathbf{r})|^{p_{\text{reference}}}_{p_{\text{actual}}}$ were generated with Bloch simulations (see Equation [4]) for a target FA of $\alpha_t = 10°$, for the 361 solutions obtained at each respiratory position for the conventional pulses as well as for the robust pulses. For each map, the normalized root-mean-square error was calculated as follows:

$$nRMSE|^{p_{\text{reference}}}_{p_{\text{actual}}} = \frac{1}{N_{p_{\text{actual}}} \cdot a_t}\sqrt{\sum_{n \in w_{p_{\text{actual}}}} \left(a_t - a(\mathbf{r}_n)|^{p_{\text{reference}}}_{p_{\text{actual}}}\right)^2}. \quad [7]$$

Here, $N_{p_{\text{actual}}}$ denote the number or voxels in ROI $w_{p_{\text{actual}}}$. The RF pulse amplitude was normalized such that the average FA for the reference position, i.e. $a(\mathbf{r})|^{\text{exhale}}_{\text{exhale}}$ for the standard pulse design, as well as $a(\mathbf{r})|^{(\text{exhale,inhale})}_{\text{exhale}}$ and $a(\mathbf{r})|^{(\text{exhale,inhale})}_{\text{inhale}}$ for the robust design, matches the target FA of 10°. Note that, in the Results section, *nRMSE* will be expressed in percent.

In situations when high RF power levels are utilized to achieve small $nRMSE|^{exhale}_{exhale}$ values, small changes of a few percent are of significantly higher importance compared with excitations with larger $nRMSE|^{exhale}_{exhale}$ values. Therefore, relative changes in *nRMSE* were also calculated for the conventional RF pulses:

$$R^{half\text{-}inhale}_{exhale} = \frac{nRMSE|^{exhale}_{half\text{-}inhale}}{nRMSE|^{exhale}_{exhale}},\ R^{inhale}_{exhale} = \frac{nRMSE|^{exhale}_{inhale}}{nRMSE|^{exhale}_{exhale}}. \quad [8]$$

For the two-spoke pulses, nRMSE, E_n, and $E_{\max}$ are displayed in polar coordinates as a function of the spoke radius k_r and the spoke angle φ.

SAR Calculation

Electromagnetic simulations of the 16-channel transceiver coil loaded with a body model at exhale respiratory position were performed using a finite difference time domain solver (Remcom, Pittsburgh, Pennsylvania, USA). Based on the resulting electromagnetic fields, the same conventional RF pulse optimization was performed as for the in vivo CINE acquisition, and global and local 10-g average SAR were calculated using identical sequence parameters. The lack of body electromagnetic models for other respiratory positions made it impossible to perform numerical simulations (including SAR) using the respiration robust RF pulse design. Therefore, to ensure safe in vivo operation in compliance with International Electrotechnical Commission (IEC) guidelines (International Standard IEC 60601-2-33 2010), all experiments were obtained within conservative SAR limits: 10-g local SAR values, calculated according to the RF pulses effectively applied, amounted to 4 W/kg (global SAR: 0.33 W/kg), thus providing a safety factor of 10 toward the short-term 10-g average local SAR first level limit. Furthermore, each CINE acquisition (with a maximum duration of 30 s each) was only applied at intervals of ≥3 min, corresponding to 6-min averaged 10-g local SAR values of 0.67 W/kg providing a safety margin of a factor 30

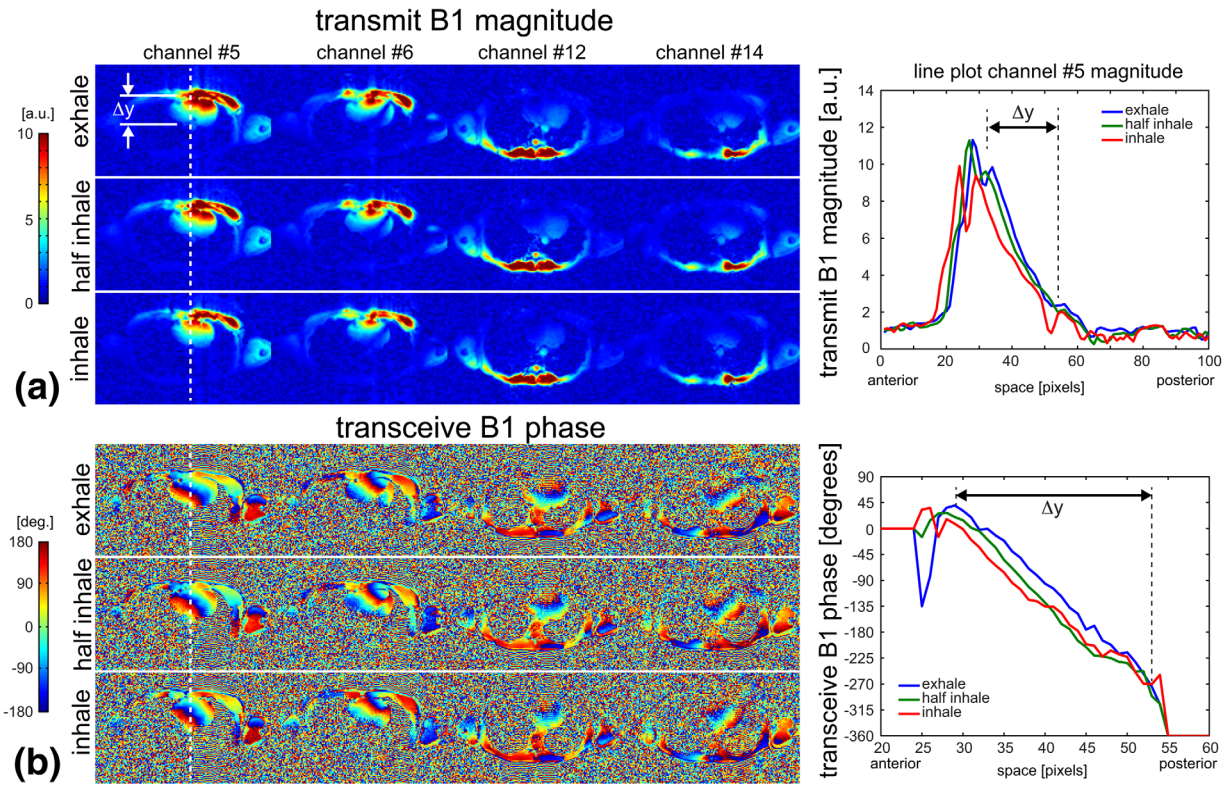

FIG. 2. Magnitude B1+ profiles (**a**) and transceive phase profiles (**b**) of the two most contributing anterior and posterior coil elements. The right diagrams show line plots along the vertical dashed lines.

compared with the 6-min first-level IEC guideline limit of 20 W/kg. These same conservative settings were applied to perform the CINE in vivo scan, using an RF excitation pulse obtained with the robust RF pulse design, which was chosen to have similar energy (102%) as the conventional RF pulse. In this study, the configuration of our pTX system imposed a same absolute upper limit in RF power for each of the 16 channels; therefore, the RF energy was identically limited for each channel (rather than considering the maximum sum of RF energy through the 16 channels).

CINE Acquisition

A comparison between conventional and robust pulse design was performed in vivo using two-spoke RF pulses with an ECG-triggered CINE acquisition in transverse view at three breath-hold positions: exhale, half-inhale, and inhale. The pTX solution to be applied was determined as follows: an energy level is determined such that the excitation is feasible within the conservative RF power limit settings. Then several solutions with nRMSE close to its lowest value are chosen along this threshold and – in order to satisfy the channel-wise uniform upper limit – the solution showing the lowest E_{max} (defined channel-wise) is retained. This approach allows to easily determine a practical tradeoff between nRMSE and E_n while limiting E_{max}. In practice, λ values between 5 and 20 are utilized to achieve nRMSE values in the order of 10% and below. Typically, nRMSE values of about 15% and above tend to show areas with significant signal amplitude reduction, particularly in posterior heart regions.

CINE acquisitions were performed using the following parameters: TE/TR = 2.6/44.8 ms; echo spacing = 5.6 ms; eight segments; 25 cardiac phases; bandwidth = 554 Hz/pixel; matrix = 192 × 124; resolution = 2.3 × 2.3 × 5 mm^3; GRAPPA = 2.

RESULTS

Impact of Respiration on Conventional One-Spoke and Two-Spoke RF Pulse Design

Figure 1a illustrates variations of the diaphragm in navigator images obtained at different respiratory positions in a representative subject. For each position, Figure 1b shows the magnitude of the corresponding GRE B_0 calibration scans in transversal, short axis, and pseudo-four-chamber views. Note that these images were all acquired with a same static B_1^+ phase shim setting optimized for $|B_1^+|$ homogeneity at exhale position in transverse view, which explains the presence of areas of low $|B_1^+|$ in short axis and four-chamber views. The transverse images illustrate a reduction of contrast homogeneity with increasing respiration, suggesting alterations of B_1^+ and/or B_0 with different respiratory positions.

The B_1^+ magnitude changes with respiration position are illustrated in Figure 2a for two anterior and two posterior coil elements. Line plots through the heart along the dashed line in channel 5 (Fig. 2a, right plot) revealed

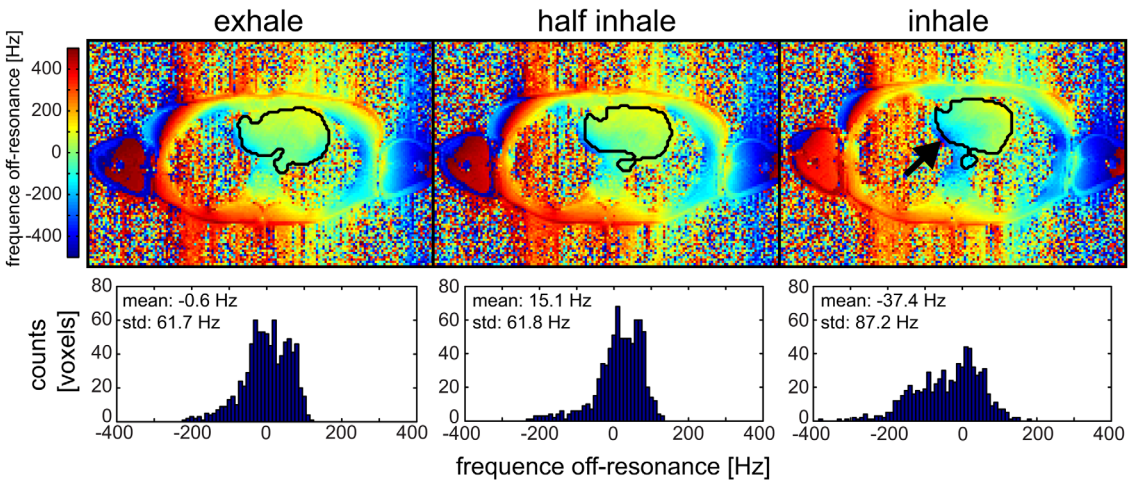

FIG. 3. ΔB_0 variations for three different respiratory positions shown for the same subject as in Figure 2. Corresponding histograms below the maps illustrate ΔB_0 distributions within the respective ROIs.

a shift of the profile toward the anterior side resulting in a $|B_1^+|$ reduction of up to 30% between exhale and inhale. The spatial transceiver phase profiles also vary with respiration, as shown in Figure 2b (note that ΔB_0-induced phase variations have been subtracted from these plots), and the corresponding line plots reveal an evolution of the transceiver phase of up to 33° between exhale and half-inhale and 55° between exhale and inhale as measured in the anterior part of the heart (position = 35 in the plot). The variations of ΔB_0 within the ROI during the respiration cycle can be appreciated on ΔB_0 maps and histograms shown in Figure 3. Although the mean ΔB_0 value changes only moderately (~37 Hz) between exhale and inhale, local ΔB_0 variations (see arrow) can reach up to more than 100 Hz, which is also reflected in an increase of the standard deviation from 62 to 87 Hz.

Figure 4 summarizes the impact of respiration-induced ΔB_0 and B_1^+ alterations on two-spoke RF pulses that were designed based on calibration scans at exhale position. The trade-off curve between E_n and $nRMSE|_{exhale}^{exhale}$ for two-spoke RF pulse optimization is shown in Figure 4a. Each cross denotes an optimized result for one λ value (unique color) and one out of 361 two-spoke trajectories, and the dashed L-shaped line follows the hull spanned by all solutions. Figure 4b and 4c shows the same data for λ = 10 and λ = 100, where the color of each point reflects the value of $nRMSE|_{inhale}^{exhale}$. Three particular solutions are highlighted (see arrows). Setting 1, obtained by minimizing equation [1] for λ = 10, provides excellent B_1^+ homogeneity for the exhale position (Fig. 4d, top row, left), with $nRMSE|_{exhale}^{exhale}$ = 6.7%. However, the high $nRMSE|_{inhale}^{exhale}$ value of 25.2% generated by this solution demonstrates that choosing the optimal solution for a given λ at exhale does not guarantee excitation fidelity robustness against changes in the respiration position. By opposition, setting 2 reflects the solution with the smallest $nRMSE|_{inhale}^{exhale}$ value (13.9%) for λ = 10, but this solution requires more energy and also has a higher $nRMSE|_{exhale}^{exhale}$ of 7.1%. If higher λ values such as λ =100 are chosen, the solution that minimizes Equation [1] (setting 3) tends to be grouped closer to the minimum $nRMSE|_{inhale}^{exhale}$ value (Fig. 4c). However, such a solution could not be utilized for imaging because of the poor B_1^+ patterns (Fig. 4d, lower row). Figure 4e and 4f illustrate the overall trend that smaller λ values yielding better excitation homogeneity result in a wide range of sensitivity to respiration induced degradation, whereas the less homogeneous B_1^+ patterns obtained with larger λ values are less affected by respiration. These effects are even more apparent when plotting the ratio $nRMSE|_{inhale}^{exhale}/nRMSE|_{exhale}^{exhale}$, as shown in Figure 4g. Similar observations were made for one-spoke excitations (Supporting Figure S1).

Analysis of 2-Spoke Pulses in Polar Coordinates

The values of E_n, E_{max}, and nRMSE are displayed in Figure 5a, in color scale, as a function of the two spokes locations given in polar excitation k-space coordinates k_r and ϕ (Fig. 5b). As before, RF pulses were designed based on exhale calibration maps, while nRMSE values were calculated from Bloch simulations for all respiratory positions. Significant variations in E_n, E_{max}, and nRMSE were observed as a function of the spoke placement, with the corresponding maximum, minimum, mean, and median values listed below each polar plot. The results in the left column were obtained with ΔB_0 deliberately set to 0 for optimization and simulation, resulting in a 180° rotational symmetry: here, pulse optimization was independent of RF timing, and a permutation of the two spokes achieved the same result (see Eq. [2]). The optimal spoke positions were located approximately along the 0°–180° axis, as seen for the $nRMSE|_{exhale}^{exhale}$ and E_n plots, which is explained by the coils' B_1^+ variations predominately oriented along the anterior–posterior direction. However, solutions along this axis were susceptible to respiration, and the optimal locations for $nRMSE|_{half\text{-}inhale}^{exhale}$, as well as those for $nRMSE|_{inhale}^{exhale}$, showed a clockwise twist as the

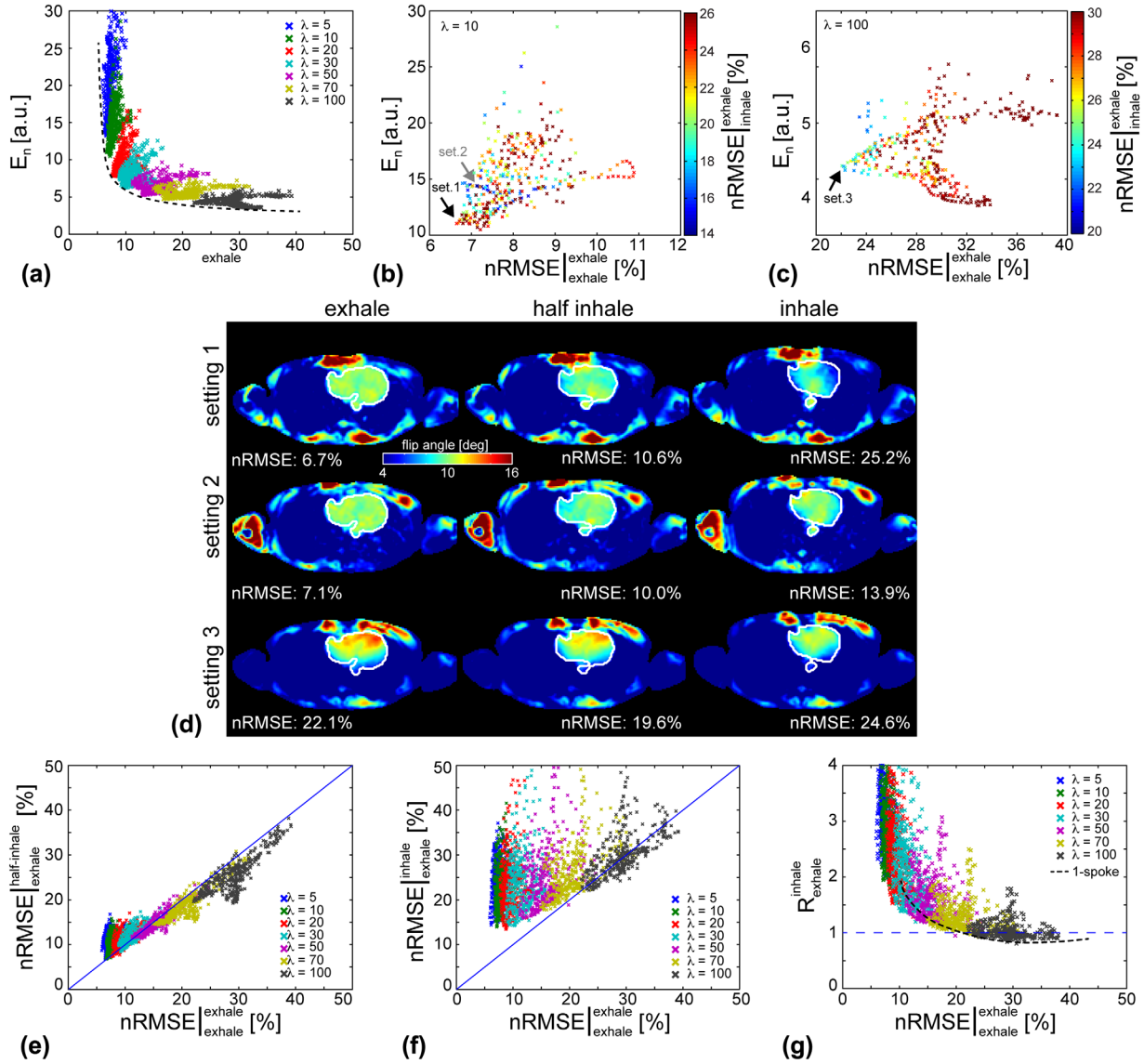

FIG. 4. **a:** Two-spoke optimization curve between Energy (E_n) and $nRMSE|^{exhale}_{exhale}$ optimized for 361 different spoke trajectories and seven different trade-off parameters λ. The same data are illustrated for λ = 10 (**b**) and λ = 100 (**c**), and the colors represents the $nRMSE|^{exhale}_{inhale}$ values. **d:** Bloch simulations for three different solutions marked in panels b and c for the three different respiratory positions. **e, f:** Absolute changes of nRMSE with different breathing positions are shown for $nRMSE|^{exhale}_{half\text{-}inhale}$ (e) and $nRMSE|^{exhale}_{inhale}$ (f). **g:** Relative changes of the nRMSE for the inhale position displayed as $R|^{inhale}_{exhale}$.

respiration volume increased. The solution characterized by $k_r = 0$ (both spokes applied at the k-space center) was energy efficient with $E_n = 12.1$ and $E_{max} = 2.9$ but had the highest excitation inhomogeneity with $nRMSE|^{exhale}_{exhale} = 11.9\%$. Including ΔB_0 in optimization and in Bloch simulation (Fig. 5a, right column) led to a loss of the rotational symmetry of the results, but had only a marginal effect on either mean or median *nRMSE* values for different respiratory positions. To better characterize the potential impact of neglecting ΔB_0 in pulse design, an additional case was considered (Fig. 5c) where ΔB_0 was not included in pulse optimization (thus E_n and E_{max} are identical to Fig. 5a, left column), but was included in Bloch simulations. A general increase of the mean and median values of *nRMSE* is clearly observed, although the overall polar plot patterns preserve strong similarity with those shown in Figure 5a (right column), including the location of the observed minima and maxima. More importantly, the impact of respiration-induced ΔB_0 variations seems far less significant than that of the corresponding $|B_1^+|$ maps alterations.

Impact of Slice Orientation on Two-Spoke Pulses

The impact of slice orientation on two-spoke pulses is illustrated in Figure 6 in another volunteer (subject 2) while using four respiratory positions. Consistent with Figure 5a (subject 1), a continuous increase of *nRMSE* was observed, here for all slice orientations, as the respiratory volume increases. In transverse view, for example,

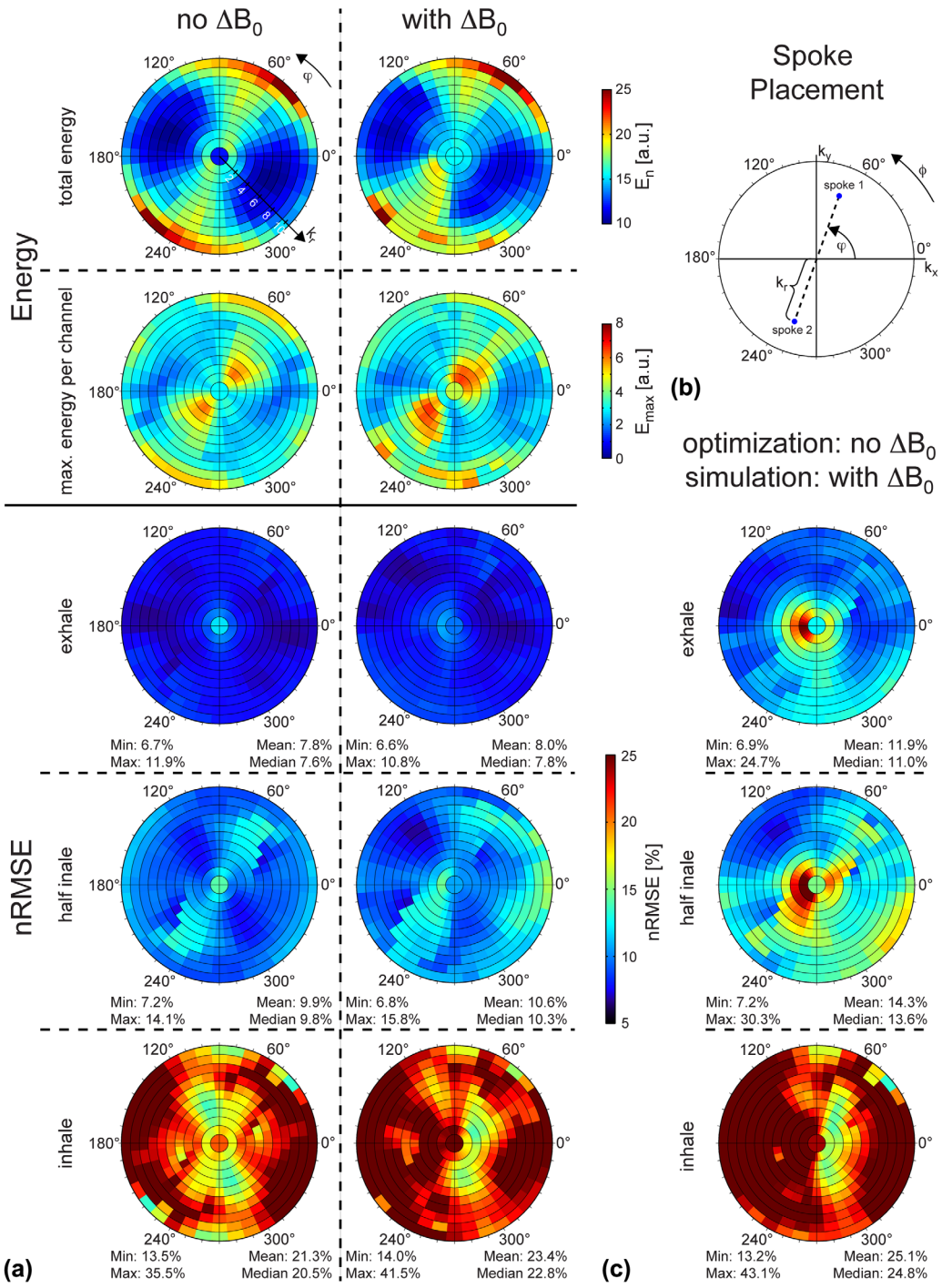

FIG. 5. **a:** E_n, E_{max}, and nRMSE values as a function of the two-spoke k-space trajectories illustrated in color in a polar coordinate system defined by the radius k_r (a) and the phase ϕ of the spokes axis as shown in **b**. In the left column in panel a, ΔB_0 is neither included in the pulse optimization nor in the Bloch simulations, which are used for the nRMSE calculation. In the right column, ΔB_0 is included in both the optimization and the Bloch simulation. **c:** ΔB_0 was not included in the optimization, thus E_n and E_{max} are identical to the left column in panel a, but ΔB_0 was included for the Bloch simulation to calculate the corresponding nRMSE values.

the mean $nRMSE|^{exhale}_{exhale}$ amounted to 8.7%, whereas the mean $nRMSE|^{exhale}_{inhale}$ was 32.1%; for subject 1 (Fig. 5a, right column), the corresponding values were, similarly, 8.0% and 23.4%. For each orientation, two solutions are marked on the polar plots in Figure 6: 1) black circles for solutions with acceptable trade-off between $nRMSE|^{exhale}_{exhale}$ and E_n [as previously reported by Schmitter et al. (20)], but with high $nRMSE|^{exhale}_{inhale}$ values, and 2) white circles for less optimal solutions in terms of E_n and/or $nRMSE|^{exhale}_{exhale}$, but more robust against respiration. Computing the latter solutions, however, required the knowledge of *nRMSE* for all respiratory positions, which is

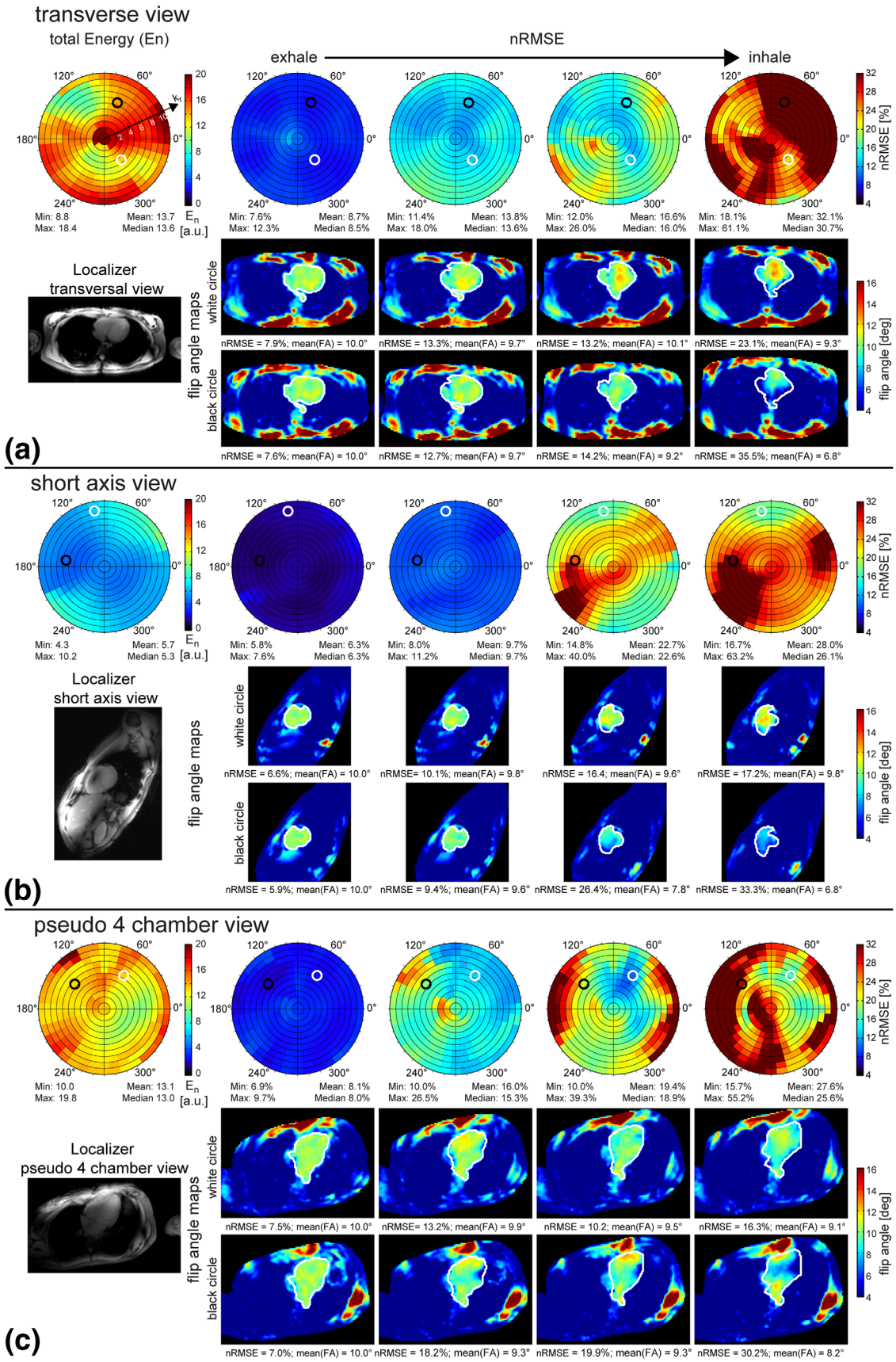

FIG. 6. Impact of the respiratory position on the excitation fidelity for two-spoke excitations optimized on exhale for different orientations: transverse view (**a**), short axis view (**b**), and pseudo-four-chamber view (**c**). For each view, E_n and nRMSE are illustrated in same coordinates as defined in Figure 5b, and the nRMSE values are shown for four different respiratory positions. For each view, two solutions (black and white circles) were chosen, and the corresponding Bloch simulations are illustrated for all four respiratory positions. The black circles mark solutions with a reasonable trade-off between a low $nRMSE|^{exhale}_{exhale}$ value and acceptable E_n, but which are sensitive to changes in the respiratory position. In contrast, the white circles mark solutions that are most robust against respiration.

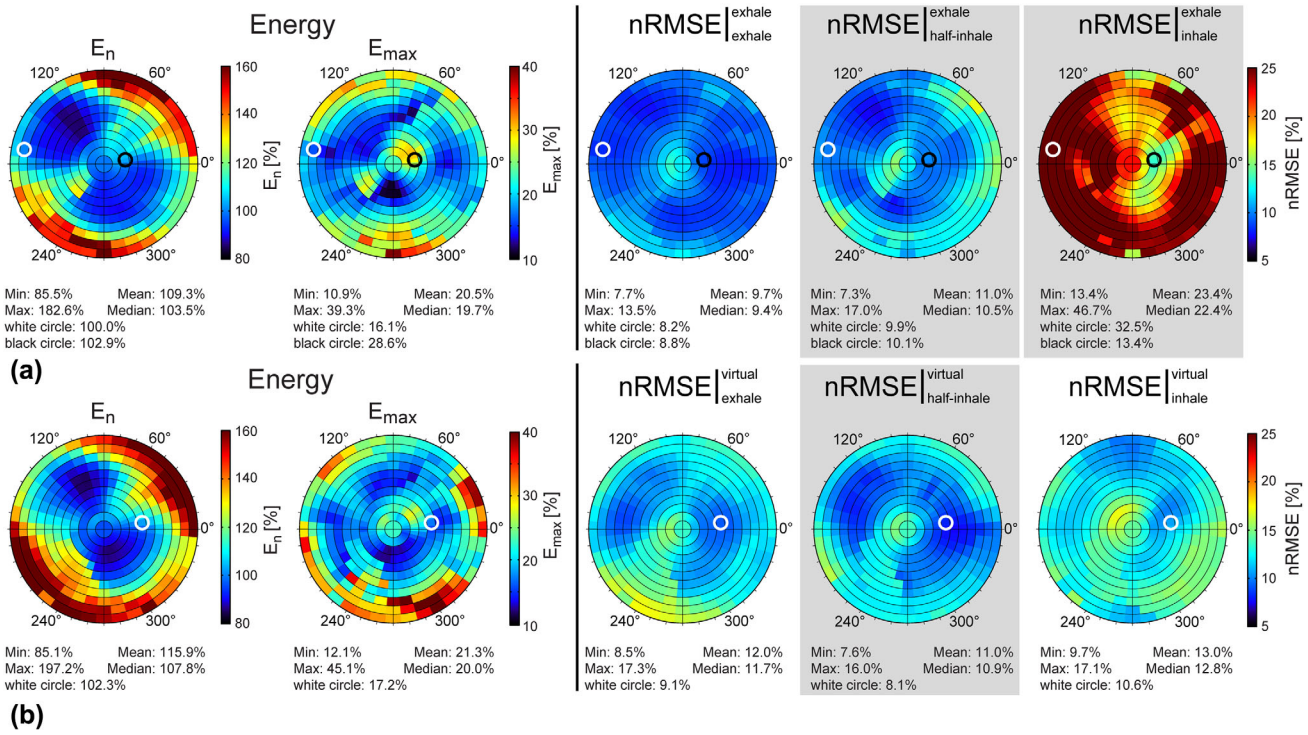

FIG. 7. **a:** E_n, E_{max}, and nRMSE values of the standard two-spoke RF pulse design, based on calibration maps obtained in the exhale position. The optimization ignores half-inhale and inhale respiratory positions, as their calibration maps are typically not acquired, here illustrated by a shaded background for the nRSME values. **b:** The proposed RF pulse design applied for two-spoke RF pulses based on calibration maps obtained in exhale and inhale, while half-inhale calibration maps are ignored (shaded background). For each RF pulse design, the white marked solution was applied in vivo (shown in Figure 8), which presents an acceptable trade-off between E_n, E_{max}, and nRMSE values (with white background only). The black circles in panel a mark solutions that are more robust against respiration-induced profile changes compared with the white solutions, but identifying these solutions requires the acquisition of calibration maps for all three respiration positions.

usually not available. Excitation patterns obtained with Bloch simulations are shown in Figure 6 for both selected solutions together with corresponding *nRMSE* and mean FA values. In transverse view, these patterns clearly revealed a stronger increase of *nRMSE* and a larger reduction of the mean FA for the black ($nRMSE|^{exhale}_{inhale}$=35.5%, FA = 6.8°) than for the white circle solution ($nRMSE|^{exhale}_{inhale}$= 23.1%, FA = 9.3°) when comparing exhale with inhale, with intermediate values for the two respiratory positions in between. Similar observation were made in short axis (Fig. 6b) and pseudo-four-chamber (Fig. 6c) views. However, in the short axis view, both the mean E_n and $nRMSE|^{exhale}_{exhale}$ values were smaller ($nRMSE|^{exhale}_{exhale}$= 6.6%, white circle) than they were in the transverse view ($nRMSE|^{exhale}_{exhale}$=7.9%, white circle), which can be attributed to a smaller ROI size and an orientation more favorable toward $|B_1^+|$ homogeneity.

Robust and Conventional RF Pulse Design Applied In Vivo

In order to demonstrate the proposed approach, conventional and robust pulses were designed based on measured calibration maps, with in vivo verification. Results of the SAR calculations corresponding to this experiment are provided in Supporting Figure S2. Pulse design results are shown for subject 1 in Figure 7, with the conventional design, labeled "design I", using exhale calibration maps (Fig. 7a), and the robust design, labeled "design II", using simultaneous calibration maps obtained at exhale and at inhale (Fig. 7b). Results for all subjects and for both designs are summarized in Tables 1 and 2. Providing that a similar range of E_n values was achieved by the two designs (Fig. 7a, left column; E_n and E_{max} are normalized to the white circled solution in a), design II resulted in a general elevation of $nRMSE|^{virtual}_{exhale}$ with a mean value of 12.0%, compared with a mean $nRMSE|^{exhale}_{exhale}$ value of 9.7% with design I. However, in clear contrast with design I, where *nRMSE* values sharply increased as the respiratory volume increased, *nRMSE* values obtained with design II remained fairly stable through the respiration cycle, as can be seen on the polar plots with corresponding numbers in Figure 7, including mean ($nRMSE|^{virtual}_{inhale}$) = 13.0% and max($nRMSE|^{virtual}_{inhale}$) = 17.1% for design II to be compared with mean ($nRMSE|^{exhale}_{inhale}$) = 23.4% and max ($nRMSE|^{exhale}_{inhale}$) = 46.7% for design I. For actual in vivo acquisition and comparison, a single solution was chosen for each design. For design I, a favorable solution was chosen similar to that described by Schmitter et al. (20), trading between E_n, E_{max}, and $nRMSE|^{exhale}_{exhale}$ (here $nRMSE|^{exhale}_{half\text{-}inhale}$ and $nRMSE|^{exhale}_{inhale}$ are ignored, indicated by a gray background shade). For design II, the trade-off considered both $nRMSE|^{virtual}_{exhale}$ and $nRMSE|^{virtual}_{inhale}$, while

Table 1
Summary of nRMSE Values with Two-Spoke Excitation in All Subjects and All Views: RF Pulses Optimized Based Only on the Exhale State

	Minimum nRMSE, %			Maximum nRMSE, %			Mean nRMSE, %		
View	Exhale	Half-Inhale	Inhale	Exhale	Half-Inhale	Inhale	Exhale	Half-Inhale	Inhale
Subject 1									
Transverse	7.7	7.3	13.4	13.5	17.0	46.7	9.7	11.0	23.4
Short axis	7.8	7.0	13.3	12.5	23.3	56.4	8.6	10.4	24.5
Four-chamber	6.9	9.1	12.4	10.5	15.4	40.6	8.6	12.3	18.4
Subject 2[a]									
Transverse	7.6	11.4	18.1	12.3	18.0	61.1	8.7	13.8	32.2
Short axis	5.8	8.0	16.7	7.6	11.2	63.2	6.3	9.7	28.0
Four-chamber	6.9	10.9	10.0	9.7	26.5	39.3	8.1	16.0	19.5
Subject 3									
Transverse	6.7	13.1	15.7	16.3	36.1	48.2	9.7	21.9	28.7
Short axis	6.1	10.4	17.0	12.3	37.7	64.8	7.9	17.2	29.1
Four-chamber	6.9	10.0	15.7	9.7	26.5	55.2	8.1	16.0	27.6
Subject 4									
Transverse	7.0	9.1	10.7	10.5	20.3	32.0	8.4	12.8	17.7
Short axis	7.8	11.3	17.7	12.1	19.7	38.2	8.9	13.8	26.1
Four-chamber	7.8	9.4	9.9	17.5	20.0	32.2	9.7	13.0	15.4
Subject 5									
Transverse	8.5	18.4	18.5	15.9	44.7	56.4	9.8	27.3	31.3
Short axis	8.5	14.4	15.7	14.4	42.3	52.0	10.5	23.6	28.1
Four-chamber	7.1	15.7	15.5	13.4	33.9	64.5	8.3	20.7	25.6

[a]In subject 2, in whom four different respiratory positions were investigated, the half-inhale values denote the respiratory position of 33% inhale.

aiming to achieve E_n and E_{max} values similar to those in design I. The resulting Bloch simulations and the corresponding actual in vivo acquisitions are shown in Figure 8 for both designs. With design I, the image quality was already compromised at half-inhale, with signal drop visible on the rightmost ventricular wall (see arrow), and stronger image degradation occurred at inhale. By contrast, image contrast and homogeneity remained essentially preserved through the respiration cycle with design II, with *nRSME* values of 9.1%, 8.1%, and 10.6% for exhale, half-inhale, and inhale, respectively. Further optimization (e.g., by relaxing the energy constraint) may

Table 2
Summary of nRMSE Values with Two-Spoke Excitation in All Subjects and All Views: RF Pulses Optimized Based on Both the Exhale and the Inhale State

	Minimum nRMSE, %			Maximum nRMSE, %			Mean nRMSE, %		
View	Exhale	Half-Inhale	Inhale	Exhale	Half-Inhale	Inhale	Exhale	Half-Inhale	Inhale
Subject 1									
Transverse	7.4	8.7	7.3	10.8	16.4	11.9	8.8	10.8	8.8
Short axis	5.8	6.4	7.0	8.8	14.4	10.1	6.8	9.0	7.9
Four-chamber	6.1	8.2	7.8	10.1	15.1	12.2	7.7	11.3	9.6
Subject 2[a]									
Transverse	7.6	11.5	10.0	15.2	19.8	17.4	10.5	14.6	13.2
Short axis	5.1	7.3	7.4	9.9	12.6	13.2	6.0	9.1	8.8
Four-chamber	6.5	10.1	7.8	10.9	19.5	12.7	8.9	13.8	9.6
Subject 3									
Transverse	5.9	9.7	8.7	14.0	26.1	18.7	8.5	16.5	11.5
Short axis	6.1	7.7	6.4	17.8	26.9	16.7	7.8	12.5	10.2
Four-chamber amber	8.0	11.7	8.2	15.6	26.0	17.2	10.5	17.9	11.4
Subject 4									
Transverse	5.5	7.1	7.4	9.8	15.5	12.1	7.1	10.1	9.5
Short axis	5.3	7.0	6.6	10.9	12.7	10.3	6.8	9.6	8.2
Four-chamber	6.4	7.4	6.2	16.4	15.0	11.3	8.3	9.4	8.0
Subject 5									
Transverse	11.0	14.5	10.1	21.6	26.9	17.7	12.7	17.6	13.1
Short axis	9.7	11.9	8.4	18.3	30.1	19.8	12.1	15.1	12.0
Four-chamber	7.0	11.9	9.3	17.4	26.2	22.9	8.4	14.6	11.6

[a]In subject 2, where four different respiratory positions were investigated, the half-inhale values denote the respiratory position of 33% inhale.

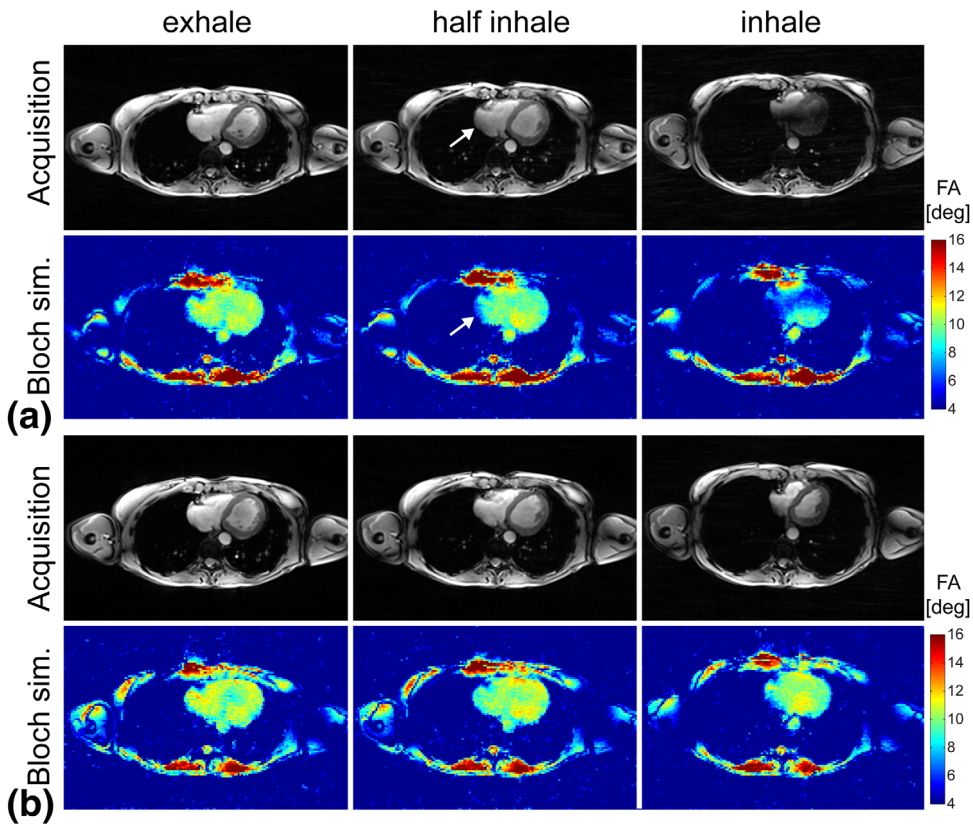

FIG. 8. Acquisitions and corresponding Bloch simulations for a) the standard two-spoke RF pulse design (**a**) and the new two-spoke RF pulse design robust against respiration (**b**). The corresponding solutions are marked by white circles in Figure 7. Degradation can be identified already for the half-inhale respiratory state as indicated by the white arrows.

be needed to address the limited signal drop still visible at inhale on the rightmost ventricular wall. The proposed design II approach appeared to be fairly more robust than picking another solution with design I, assuming that $nRMSE|_{inhale}^{exhale}$ was known: for example, the black circled solutions shown in Figure 7a might seem to be a preferred choice, but this solution required significantly higher E_{max} (28.6%) and resulted in higher $nRMSE|_{inhale}^{exhale}$ (13.4%) compared with the solution in design II (17.2% and 10.6%, respectively).

DISCUSSION AND CONCLUSIONS

The purpose of this study was to investigate the impact of respiration on cardiac RF pulse design using either one-spoke (equivalent to B_1^+ shimming with phase and magnitude optimization) or two-spoke pTX excitation. For this study, we modified B_1^+ and B_0 mapping sequences in order to include interleaved navigator images of the diaphragm.

RF pulses are usually designed based on one set of calibration maps obtained in a single physiological condition, including the respiratory position. When subsequently applied at different phases of the respiration cycle, such RF pulses can result in substantial deviations of the excitation pattern. We identified two predominant sources of respiration-induced errors: 1) the alteration of the B_1^+ profiles (magnitude and phase) of the transmit coil elements during the respiratory cycle and 2) the use of small regularization weight in RF pulse optimization yielding higher excitation fidelity but relatively larger sensitivity to respiration quantified by R_{exhale}^{inhale}. Interestingly, respiration-induced variations of B_0 only had a marginal impact on excitation patterns, even though they altered the optimal two-spoke positions in excitation k-space. The same overall trend was observed for all orientations (transverse, short axis, or four-chamber view), with excitation pattern alterations already visible at half-inhale and more pronounced at inhale using conventional RF pulse design based on B_1^+/B_0 calibration at exhale. Similar results were obtained in all five subjects investigated in the study, as listed in Table 1.

These excitation defects can have a significant impact on cardiovascular applications, as shown here in cardiac CINE acquisitions. Many of these applications rely on breath-hold acquisitions (28), and our observations indicate that, even with careful breath-hold instructions, significant variations of respiratory position may occur for some subjects between subsequent breath-holds, resulting in a mismatch between B_1^+/B_0 calibration and actual imaging scans. Instability between breath-holds is a known issue (29); one way to ensure excitation profile consistency is to include a navigator prior to the imaging scan and discard images based on the diaphragm position determined by the navigator. Alternatively, different pTX RF pulses could be designed for different respiratory positions, and the actual RF pulse to be played out be determined by the navigator image collected prior to each imaging scan.

In this study, we present a simpler approach using a novel RF pulse design that includes calibration maps obtained at multiple respiratory positions. These maps

are assembled as a group of virtual slices that are optimized simultaneously over the target region, resulting in pTX RF pulses robust against respiration induced errors. This design is not restricted to degradation caused by respiration; it can also be applied to other (periodic) changes of the physiological state that alter B_1^+ maps. Here, we apply this formalism on respiration robust one-spoke cardiac imaging and expand this approach toward two-spoke pTX pulses that have been shown capable of improving further image homogeneity at 7T (20). Similar to previous work, we used one-spoke excitation initialized with different starting phase patterns and investigated two-spoke excitations with symmetric placement in k-space; this symmetric k-space approach, which has demonstrated high-quality cardiac images at 7T, offers the advantage of being less sensitive if the RF pulses are scaled to larger FA (30) and allows a straightforward visualization of optimization results as a function of spoke positions. We also investigated an asymmetric spoke placement as well as three spoke excitations. Overall, both approaches did not improve the sensitivity toward respiration. It should be noted, however, that lower numbers of spokes are preferable, because cardiac RF pulses are typically fairly short; RF pulse durations from the vendor's standard sequence are between 0.6 and 2 ms, and those durations are increasingly challenging to achieve with rising numbers of spokes. However, the framework presented in this study is not limited to spokes or slice-selective pulses: it can be applied to three-dimensional slab-selective (25), localized (31), or nonselective (32) pTX RF pulses, as well as to simultaneous multislice pTX acquisitions ("pTX multiband") (33–35) recently demonstrated in cardiac CINE acquisitions at 7T (36). Furthermore, other regularization terms such as local or global SAR constraints can be included in the optimization (37).

It is well-known that respiration changes the heart position within the body (compare, e.g., Fig. 8). To follow heart motion with respiration, slice tracking techniques are often applied based on the diaphragm position using a typical scaling factor of 0.6 (38). In one subject, we investigated respiration-induced excitation pattern changes, including slice tracking with different factors between 0 and 1.5. Slice tracking did not significantly change the polar plot pattern; however, $nRMSE|_{inhale}^{exhale}$ values overall tended to increase with increasing tracking factor.

In this study, we used a 16-channel transceiver TEM stripline coil (26), and we investigated via noise correlation analysis coupling variations between coil elements during respiration. In subject 1, the coupling values ranged from −10 dB between next neighboring coil elements down to −46 dB for elements furthest apart. The largest change in coupling values between exhale and inhale were observed on the two frontal channels that contribute the most to cardiac coverage (#5 and #6; see Fig. 2), where the coupling value changed from −19.5 dB to −24.4 dB. Similar values were observed in the other subjects with a maximum range of changes from −23.8 dB to −32.3 dB, occurring between the same two frontal channels, in subject 3. It will be interesting in future studies to compare these results using different RF coil structures, such as loops (39) or radiative antennas (40).

The proposed RF pulse design is not limited to breath-hold applications. In practice, a variety of medical conditions preclude single or multiple breath-hold scans, and acquisitions are therefore performed under free breathing. This is the case, for example, in children with congenital heart disease and in patients with arrhythmia who may not able to perform breath-holds, as well as in some elderly people who may have difficulties hearing breath-hold instructions. For these patients, the proposed algorithm could strongly improve image quality, based on the modified calibration scans with navigator images prior to each image, compatible with free-breathing as well. In the latter case, calibration maps could be acquired during a few training breathing cycles and retrospectively reordered according to the respiratory position or prospectively acquired using the navigator image information. In other clinical situations, active respiration is necessary for diagnostic purposes. In constrictive pericardial disease, pathological ventricular coupling can lead to an abnormal motion or bending of the septum, which is highly dependent on respiration, requiring fast two-dimensional acquisitions to be performed while the patient is asked to breathe deeply in and out (28,41). For these acquisitions, reduction of the FA and impaired contrast homogeneity may be expected, as demonstrated in the present study. In addition to patient restrictions, many sequences cannot be performed during breath-hold due to long scan times. Commonly, those acquisitions use respiration navigator tracking that discard images that are outside the navigator acceptance window, which typically achieve acceptance efficiencies between 30% and 50%. However, recently there have been significant advances in increasing two-dimensional or three-dimensional scan efficiency up to 100% (i.e., using data of the entire respiratory cycle) for coronary MR angiography (3,42,43), cardiac perfusion (44,45), or cardiac CINE acquisitions (46) while prospectively or retrospectively correcting for respiratory motion. Weingartner et al. (47) reported a three-dimensional cardiac T_1 mapping approach that uses 100% scan efficiency for outer k-space lines and a reduced efficiency on the inner k-space part. Furthermore, improved hardware and novel acceleration techniques contribute to enable free-breathing real-time cardiac imaging with temporal resolutions below 50 ms, as demonstrated by several groups (4,5,48).

Although all these methods were demonstrated at lower field strength than the current 7T study, they underscore the importance of being able to preserve cardiac image quality throughout the entire respiratory cycle. It should be emphasized that, even at 3T, heterogeneous B_1^+ and B_0 patterns can have a significant impact on image quality, which has resulted in the recent development of clinical 3T pTX scanners operating with two transmit channels, with improved flip angle homogeneity for cardiac applications (49). In the context of ultrahigh fields, where CMR can benefit from longer T_1 relaxation, higher signal-to-noise ratio, and better parallel imaging performance, addressing respiration-induced excitation profile degradations with the

proposed robust RF pulse design is expected to have a substantial impact on potential clinical outcome.

ACKNOWLEDGMENTS

We thank Jinfeng Tian (University of Minnesota, Minneapolis, Minnesota, USA) for calculating the RF coil electromagnetic model used in this study.

REFERENCES

1. Paling MR, Brookeman JR. Respiration artifacts in MR imaging: reduction by breath holding. J Comput Assist Tomogr 1986;10:1080–1082.
2. Ehman RL, Felmlee JP. Adaptive technique for high-definition MR imaging of moving structures. Radiology 1989;173:255–263.
3. Bhat H, Ge L, Nielles-Vallespin S, Zuehlsdorff S, Li D. 3D radial sampling and 3D affine transform-based respiratory motion correction technique for free-breathing whole-heart coronary MRA with 100% imaging efficiency. Magn Reson Med 2011;65:1269–1277.
4. Feng L, Srichai MB, Lim RP, Harrison A, King W, Adluru G, Dibella EV, Sodickson DK, Otazo R, Kim D. Highly accelerated real-time cardiac cine MRI using k-t SPARSE-SENSE. Magn Reson Med 2013;70:64–74.
5. Zhang S, Uecker M, Voit D, Merboldt KD, Frahm J. Real-time cardiovascular magnetic resonance at high temporal resolution: radial FLASH with nonlinear inverse reconstruction. J Cardiovasc Magn Reson 2010;12:39.
6. Oshinski JN, Delfino JG, Sharma P, Gharib AM, Pettigrew RI. Cardiovascular magnetic resonance at 3.0 T: current state of the art. J Cardiovasc Magn Reson 2010;12:55.
7. Schar M, Kozerke S, Fischer SE, Boesiger P. Cardiac SSFP imaging at 3 Tesla. Magn Reson Med 2004;51:799–806.
8. Sung K, Nayak KS. Measurement and characterization of RF nonuniformity over the heart at 3T using body coil transmission. J Magn Reson Imaging 2008;27:643–648.
9. Niendorf T, Sodickson DK, Krombach GA, Schulz-Menger J. Toward cardiovascular MRI at 7 T: clinical needs, technical solutions and research promises. Eur Radiol 2010;20:2806–2816.
10. Rodgers CT, Piechnik SK, Delabarre LJ, Van de Moortele PF, Snyder CJ, Neubauer S, Robson MD, Vaughan JT. Inversion recovery at 7 T in the human myocardium: measurement of T(1), inversion efficiency and B(1) (+). Magn Reson Med 2013;70:1038–1046.
11. Snyder CJ, DelaBarre L, Metzger GJ, van de Moortele PF, Akgun C, Ugurbil K, Vaughan JT. Initial results of cardiac imaging at 7 Tesla. Magn Reson Med 2009;61:517–524.
12. Suttie JJ, Delabarre L, Pitcher A, et al. 7 Tesla (T) human cardiovascular magnetic resonance imaging using FLASH and SSFP to assess cardiac function: validation against 1.5 T and 3 T. NMR Biomed 2012; 25:27–34.
13. Vaughan JT, Snyder CJ, DelaBarre LJ, Bolan PJ, Tian J, Bolinger L, Adriany G, Andersen P, Strupp J, Ugurbil K. Whole-body imaging at 7T: preliminary results. Magn Reson Med 2009;61:244–248.
14. Vaughan JT, Garwood M, Collins CM, et al. 7T vs. 4T: RF power, homogeneity, and signal-to-noise comparison in head images. Magn Reson Med 2001;46:24–30.
15. Wiesinger F, Van de Moortele PF, Adriany G, De Zanche N, Ugurbil K, Pruessmann KP. Parallel imaging performance as a function of field strength—an experimental investigation using electrodynamic scaling. Magn Reson Med 2004;52:953–964.
16. Rooney WD, Johnson G, Li X, Cohen ER, Kim SG, Ugurbil K, Springer CS Jr. Magnetic field and tissue dependencies of human brain longitudinal 1H2O relaxation in vivo. Magn Reson Med 2007; 57:308–318.
17. Metzger GJ, Snyder C, Akgun C, Vaughan T, Ugurbil K, Van de Moortele PF. Local B1+ shimming for prostate imaging with transceiver arrays at 7T based on subject-dependent transmit phase measurements. Magn Reson Med 2008;59:396–409.
18. Katscher U, Bornert P, Leussler C, van den Brink JS. Transmit SENSE. Magn Reson Med 2003;49:144–150.
19. Zhu Y. Parallel excitation with an array of transmit coils. Magn Reson Med 2004;51:775–784.
20. Schmitter S, DelaBarre L, Wu X, Greiser A, Wang D, Auerbach EJ, Vaughan JT, Ugurbil K, Van de Moortele PF. Cardiac imaging at 7 Tesla: single- and two-spoke radiofrequency pulse design with 16-channel parallel excitation. Magn Reson Med 2013;70:1210–1219.
21. Nehrke K, Börnert P. Free-breathing abdominal B1 mapping at 3T using the DREAM approach. In Proceedings of the 20th Annual Meeting of ISMRM, Melbourne, Australia, 2012. Abstract 3356.
22. Padormo S, Malik S, Hajnal JV, Larkman DJ. Assessing and correcting respiration induced variation of B1 in the liver. In Proceedings of the 17th Annual Meeting of ISMRM, Honolulu, Hawaii, USA, 2009. Abstract 754.
23. Grissom W, Yip CY, Zhang Z, Stenger VA, Fessler JA, Noll DC. Spatial domain method for the design of RF pulses in multicoil parallel excitation. Magn Reson Med 2006;56:620–629.
24. Setsompop K, Wald LL, Alagappan V, Gagoski BA, Adalsteinsson E. Magnitude least squares optimization for parallel radio frequency excitation design demonstrated at 7 Tesla with eight channels. Magn Reson Med 2008;59:908–915.
25. Schmitter S, Wu X, Auerbach EJ, Adriany G, Pfeuffer J, Hamm M, Ugurbil K, van de Moortele PF. Seven-tesla time-of-flight angiography using a 16-channel parallel transmit system with power-constrained 3-dimensional spoke radiofrequency pulse design. Invest Radiol 2014;49:314–325.
26. Snyder CJ, Delabarre L, Moeller S, Tian J, Akgun C, Van de Moortele PF, Bolan PJ, Ugurbil K, Vaughan JT, Metzger GJ. Comparison between eight- and sixteen-channel TEM transceive arrays for body imaging at 7 T. Magn Reson Med 2012;67:954–964.
27. Van de Moortele PF, Ugurbil K. Very Fast Multi Channel B1 Calibration at High Field in the Small Flip Angle Regime. In Proceedings of the 17th Annual Meeting of ISMRM, Honolulu, Hawaii, USA, 2009. Abstract 367.
28. Kramer CM, Barkhausen J, Flamm SD, Kim RJ, Nagel E, Society for Cardiovascular Magnetic Resonance Board of Trustees Task Force on Standardized Protocols. Standardized cardiovascular magnetic resonance (CMR) protocols 2013 update. J Cardiovasc Magn Reson 2013; 15:91.
29. Dymarkowski S. Practical set-up. In: Bogaert J, Dymarkowski S, Taylor AM, Muthurangu V, editors. Clinical cardiac MRI. Berlin, Heidelberg: Springer-Verlag; 2012. p 53–67.
30. Pauly J, Nishimura D, Macovski A. A linear class of large-tip-angle selective excitation pulses. J Magn Reson 1989;82:571–587.
31. Schneider JT, Kalayciyan R, Haas M, Herrmann SR, Ruhm W, Hennig J, Ullmann P. Inner-volume imaging in vivo using three-dimensional parallel spatially selective excitation. Magn Reson Med 2013;69: 1367–1378.
32. Cloos MA, Boulant N, Luong M, Ferrand G, Giacomini E, Le Bihan D, Amadon A. kT -points: short three-dimensional tailored RF pulses for flip-angle homogenization over an extended volume. Magn Reson Med 2012;67:72–80.
33. Larkman DJ, Hajnal JV, Herlihy AH, Coutts GA, Young IR, Ehnholm G. Use of multicoil arrays for separation of signal from multiple slices simultaneously excited. J Magn Reson Imaging 2001;13:313–317.
34. Wu X, Schmitter S, Auerbach EJ, Moeller S, Ugurbil K, Van de Moortele PF. Simultaneous multislice multiband parallel radiofrequency excitation with independent slice-specific transmit B1 homogenization. Magn Reson Med 2013;70:630–638.
35. Poser BA, Anderson RJ, Guerin B, Setsompop K, Deng W, Mareyam A, Serano P, Wald LL, Stenger VA. Simultaneous multislice excitation by parallel transmission. Magn Reson Med 2014;71:1416–1427.
36. Schmitter S, Wu X, Moeller S, Wang D, Greiser A, Auerbach E, DelaBarre L, Van de Moortele PF, Ugurbil K. Multi-band-multi-spoke pTX RF pulse design in the heart at 7 Tesla: Towards faster, uniform contrast cardiac CINE imaging. In Proceedings of the 22th Annual Meeting of ISMRM, Milan, Italy, 2014. Abstract 646.
37. Guerin B, Gebhardt M, Cauley S, Adalsteinsson E, Wald LL. Local specific absorption rate (SAR), global SAR, transmitter power, and excitation accuracy trade-offs in low flip-angle parallel transmit pulse design. Magn Reson Med 2014;71:1446–1457.
38. Wang Y, Riederer SJ, Ehman RL. Respiratory motion of the heart: kinematics and the implications for the spatial resolution in coronary imaging. Magn Reson Med 1995;33:713–719.
39. Graessl A, Renz W, Hezel F, et al. Modular 32-channel transceiver coil array for cardiac MRI at 7.0T. Magn Reson Med 2014;72:276–290.
40. Raaijmakers AJ, Ipek O, Klomp DW, Possanzini C, Harvey PR, Lagendijk JJ, van den Berg CA. Design of a radiative surface coil array element at 7 T: the single-side adapted dipole antenna. Magn Reson Med 2011;66:1488–1497.
41. Francone M, Dymarkowski S, Kalantzi M, Bogaert J. Real-time cine MRI of ventricular septal motion: a novel approach to assess ventricular coupling. J Magn Reson Imaging 2005;21:305–309.

42. Pang J, Sharif B, Arsanjani R, Bi X, Fan Z, Yang Q, Li K, Berman DS, Li D. Accelerated whole-heart coronary MRA using motion-corrected sensitivity encoding with three-dimensional projection reconstruction. Magn Reson Med 2015;73:284–291.
43. Prieto C, Doneva M, Usman M, Henningsson M, Greil G, Schaeffter T, Botnar RM. Highly efficient respiratory motion compensated free-breathing coronary mra using golden-step Cartesian acquisition. J Magn Reson Imaging 2015;41:738–746.
44. Schmidt JF, Wissmann L, Manka R, Kozerke S. Iterative k-t principal component analysis with nonrigid motion correction for dynamic three-dimensional cardiac perfusion imaging. Magn Reson Med 2014; 72:68–79.
45. Basha TA, Roujol S, Kissinger KV, Goddu B, Berg S, Manning WJ, Nezafat R. Free-breathing cardiac MR stress perfusion with real-time slice tracking. Magn Reson Med 2014;72:689–698.
46. Leung AO, Paterson I, Thompson RB. Free-breathing cine MRI. Magn Reson Med 2008;60:709–717.
47. Weingartner S, Akcakaya M, Roujol S, Basha T, Stehning C, Kissinger KV, Goddu B, Berg S, Manning WJ, Nezafat R. Free-breathing post-contrast three-dimensional T mapping: volumetric assessment of myocardial T values. Magn Reson Med 2015;73:214–222.
48. Seiberlich N, Ehses P, Duerk J, Gilkeson R, Griswold M. Improved radial GRAPPA calibration for real-time free-breathing cardiac imaging. Magn Reson Med 2011;65:492–505.
49. Krishnamurthy R, Pednekar A, Kouwenhoven M, Cheong B, Muthupillai R. Evaluation of a subject specific dual-transmit approach for improving B1 field homogeneity in cardiovascular magnetic resonance at 3T. J Cardiovasc Magn Reson 2013;15:68.

SUPPORTING INFORMATION

Additional Supporting Information may be found in the online version of this article.

Supporting Figure S1. a) 1-spoke optimization curve between Energy (En) and $nRMSE|^{exhale}_{exhale}$ for different tradeoff parameters λ. The diagram reveals two different L-curves, among which the curve closer to the origin describes acceptable solutions while the upwards shifted curve reflects solutions with a pronounced $|B1+|$ minimum within the ROI. Two examples (setting 1 and 2) marked in a) are shown in b) for three different respiratory positions. Changes of nRMSE with different breathing positions are shown in c) for $nRMSE|^{exhale}_{half-inhale}$ (c) and $nRMSE|^{exhale}_{inhale}$ (d) as a function of $nRMSE|^{exhale}_{exhale}$ for different λ values. For these diagrams, only the acceptable solutions (lower L-curve in a) are displayed. Relative changes of the diagrams shown in c) and d) are displayed in e) as ratio values $R|^{half-inhale}_{exhale}$ and $R|^{inhale}_{exhale}$ as a function of $nRMSE|^{exhale}_{exhale}$.

Supporting Figure S2. Top row: E_n, E_{max}, and nRMSE values as a function of the two-spoke k space trajectories in a polar coordinate system defined by the spokes location. The optimization was performed using an electromagnetic simulation dataset of the same RF coil and similar nRMSE values were targeted for the optimization as used in-vivo. Bottom row: corresponding global and 10g average local SAR values for each spoke trajectory calculated for a 10° flip angle using same RF pulse durations and same duty cycle as utilized in vivo.